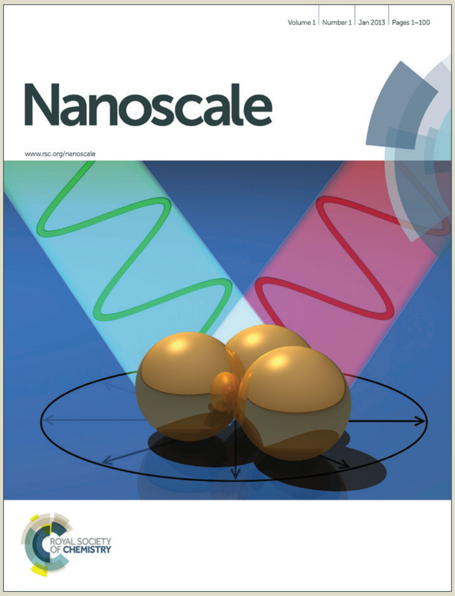

Facile synthesis of intense green-emitting $LiGdF_4$:Yb,Er-based upconversion bipyramidal nanocrystals and their polymer composites

Hyejin Na,[a] Jong Seok Jeong,[b] Hye Jung Chang,[c] Hyun You Kim,[d,e] Kyoungja Woo,[a] Kipil Lim,[a] K. Andre Mkhoyan[b] and Ho Seong Jang*,[a,f]

[a]Molecular Recognition Research Center, Korea Institute of Science and Technology, Hwarangno 14-gil 5, Seongbuk-gu, Seoul 136-791, Republic of Korea

[b]Department of Chemical Engineering and Materials Science, University of Minnesota, 421 Washington Avenue SE, Minneapolis, MN 55455, United States.

[c]Advanced Analysis Center, Korea Institute of Science and Technology, Hwarangno 14-gil 5, Seongbuk-gu, Seoul 136-791, Republic of Korea

[d]Center for Functional Nanomaterials, Brookhaven National Laboratory, Upton, New York 11973, United States.

[e]Department of Nanomaterials Engineering, Chungnam National University, 99 Daehak-ro, Yuseong-gu, Daejeon 305-764, Republic of Korea

[f]Present address: Center for Materials Architecturing, Korea Institute of Science and Technology, Hwarangno 14-gil 5, Seongbuk-gu, Seoul 136-791, Republic of Korea

* Corresponding author. E-mail: msekorea@kist.re.kr; Fax: +82-2-958-5451; Tel:+82-2-958-5263

ABSTRACT

A pathway for achieving intense green-emitting $LiGdF_4$:Yb,Er upconversion nanophosphors (UCNPs) via Y^{3+} doping was demonstrated. It was revealed that Y^{3+} doping initiated the formation of a tetragonal phase and affected the particle size. Single tetragonal-phase $LiGd_{0.4}Y_{0.4}F_4$:Yb(18%),Er(2%) ($LGY_{0.4}F$:Yb,Er) UCNPs exhibited strong upconversion (UC) green luminescence and tetragonal bipyramidal morphologies. They showed 1325 and 325-fold higher photoluminescence intensity than the 0 and 80 mol% Y^{3+}-doped $LiGdF_4$:Yb,Er UCNPs, respectively. Additionally particle size (edge length) of $LiGdF_4$:Yb,Er-based upconversion tetrahedral bipyramids (UCTBs) was controlled from 60.5 nm to ultrasmall size of 9.3 nm with varying Y^{3+} doping concentration. In an $LGY_{0.4}F$:Yb,Er UCTB, uniform distribution of all constituent elements was directly confirmed by using a high-angle annular dark-field scanning transmission electron microscopy and energy-filtered transmission electron microscopy (EFTEM) image analyses. In particular, existence of activator Er^{3+} ions with extremely small quantity was clearly seen over a particle on the EFTEM image. Moreover, the $LGY_{0.4}F$:Yb,Er UCTBs were successfully incorporated into polydimethylsiloxane (PDMS) polymer and the highly transparent UCTB-PDMS composites showed bright green light under the excitation of 980 nm infrared light.

1. Introduction

Lanthanide doping into inorganic crystals gives these materials new functionalities such as upconversion (UC),[1-3] downconversion/downshifting,[4-7] dual-mode luminescence,[8-10] enhanced computed tomography (CT) contrast[11] and magnetism.[12,13] In particular, lanthanide ion-doped (Ln^{3+}-doped) upconversion nanophosphors (UCNPs) have been in spotlight due to their excellent chemical and optical properties. The UCNPs have many advantages over conventional fluorescent organic dyes and quantum dots, such as high photostability (without photobleaching), long life time (from μs to ms) due to the luminescence attributed to parity-forbidden f-f transition, large anti-Stokes shifts, non-toxicity (no Cd or Pb), and a lack of photoblinking.[14] Moreover, the UCNPs exhibit an infrared (IR) to visible light conversion efficiency an order of magnitude higher than the two-photon absorption process. This high conversion efficiency of the UCNPs is due to the existence of a real, intermediate energy level between the ground and excited states.[14,15] Given this high UC efficiency, commercially available, inexpensive continuous-wave diode lasers can be used as an excitation light source. Recently, sub-10 nm, ultrasmall UCNPs were successfully synthesized with excellent luminescent properties that could allow further bioimaging applications.[16,17]

Until now, Ln^{3+}-doped fluoride-based UCNPs have been extensively studied, because fluoride materials have low phonon energies and show high optical transparency in the visible region due to their large band-gap energy.[18,19] In particular, $NaLnF_4$ (Ln = Gd, La, Lu, and Y)-based UCNPs have attracted great attention.[17,20-25] For example, β-$NaYF_4$ is known as the most efficient host material for blue and green upconversion luminescence.[26] On the other hand, $LiGdF_4$ is an outstanding host for downconversion luminescence with a visible quantum efficiency approaching 190%.[27] However, although $LiYF_4$:Yb,Tm/Er and $LiYF_4$:Er UCNPs have been reported,[28-31] few reports describe $LiGdF_4$-based UCNPs possibly due to the difficulty in synthesizing $LiGdF_4$ nanocrystals with a single tetragonal phase.[32] Because lanthanide doping simultaneously affects both the size and phase of the UCNPs,[33] we used Y doping as a synthetic pathway to single-phase $LiGdF_4$ UCNPs. In this article, we report on the facile synthesis of highly bright Y^{3+}-doped $LiGdF_4$:Yb,Er UCNPs with a single tetragonal phase. The Li(Gd,Y)F_4:Yb,Er showed intense green UC luminescence with higher efficiency than β-NaYF_4:Yb,Er UCNPs at 150 W/cm^2 power density and tunable size from several tens of nanometers to sub-10 nm via Y^{3+} doping. In addition, the applicability of the Li(Gd,Y)F_4:Yb,Er UCNPs to transparent display devices was examined through fabrication of transparent polymer composites.

On the other hand, one must establish a compositional map of these UCNPs and the locations of the activator Ln^{3+} ions within the particles because the luminescence of the UCNPs is strongly affected by surface defects.[34,35] Although the dopant distribution in the Ln^{3+}-doped $NaGdF_4$ has been analyzed via synchrotron X-ray photoelectron spectroscopy (XPS), determining the precise elemental distribution at the single-nanoparticle level remains difficult because XPS technique is an ensemble measurement.[36] Thus, transmission electron microscopy (TEM) combined with energy dispersive X-ray spectroscopy (EDS) and electron energy-loss spectroscopy (EELS) analysis is necessary to identify the compositional distributions within a nanoparticle. Here, for the first time, we successfully synthesized highly bright, single-phase $LiGdF_4$-based UC tetragonal bipyramids (UCTBs) via Y doping. We also provide direct identification of the elemental distribution of each constituent in the UCTBs by applying energy-filtered TEM (EFTEM) and high-angle annular dark-field scanning transmission electron microscopy (HAADF STEM).

2. Experimental

2.1. Materials

$LiOH\cdot H_2O$ (99.995%), $GdCl_3\cdot 6H_2O$ (99%), $YCl_3\cdot 6H_2O$ (99.99%), $YbCl_3\cdot 6H_2O$ (99.9%), $ErCl_3\cdot 6H_2O$ (99.9%), NH_4F (99.99+%), oleic acid (OA, technical grade 90%), and 1-octadecene (ODE, technical grade 90%) were purchased from Aldrich and they were used without further purification. Sodium oleate (> 97%) was obtained from TCI.

2.2. Synthesis of the Li(Gd,Y)F_4:Yb,Er upconversion nanophosphors

First, the lanthanide oleates [Ln(oleate)$_3$, Ln = Gd, Y, Yb, and Er] were prepared by adapting the synthesis reported by Hyeon's group.[37] Then, 1 mmol of Ln(oleate)$_3$ complexes, in which the quantities of Yb and Er were fixed at 0.18 and 0.02 mmol, respectively, were loaded into a three-necked flask containing a solvent mixture of 10.5 ml OA and 10.5 ml ODE. The mixture was heated to 150 °C for 40 min to yield a transparent solution. After the reaction mixture cooled to 50 °C, a methanol (MeOH) solution (10 ml) containing $LiOH \cdot H_2O$ (2.5 mmol) and NH_4F (4 mmol) was added to the reaction flask and then stirred for 40 min. After the MeOH was removed, the solution was heated to 320 °C for 90 min under an Ar atmosphere. The as-synthesized nanophosphors were washed several times with ethanol and dispersed in chloroform.

2.3. Preparation of the UCTB-PDMS composites

To prepare the UCTB-polydimethylsiloxane (PDMS) composites, 0.4 ml of the UCTB solution (approximately 1 wt%) was thoroughly mixed with 10 ml of SYLGARD silicone elastomer 184 followed by the addition of a curing agent (1 ml). Finally, the UCTB-PDMS composites (approximately 0.04 wt% UCTB) were aged overnight and then heat-treated at 80 °C for 1 h.

2.4. Characterization

The absorption and transmittance spectra were obtained using a Perkin-Elmer Lambda25 UV/VIS spectrophotometer. The absorption spectrum of the UCNP chloroform solution (~ 1wt%) in quartz cuvette (1 cm × 1 cm, Hellma QS cell) was obtained under the condition of 240 nm/min of scan speed and 1 nm of slit width. The crystal structures of the as-synthesized nanophosphors were determined using a Bruker D8 ADVANCE diffractometer with Cu K_α radiation at 40 kV and 40 mA. The Photoluminescence (PL) spectra were collected using a Hitachi F-7000 spectrophotometer. The scanning electron microscopy (SEM) and TEM images were obtained on an FEI Nova nanoSEM operated at 10 kV and a Tecnai G2 F20 operated at 200 kV, respectively. The EFTEM images were obtained on an FEI Titan 80/300 operated at 300 kV equipped with a GIF Quantum®ERS (Gatan, Inc., USA). The high-resolution STEM (HR-STEM) images were obtained using an FEI Tecnai G2 F30 S-TEM operated at 300 kV.

2.5. Density functional theory (DFT) calculation

We performed spin-polarized density functional theory (DFT) calculation in a plane-wave basis with the Vienna Ab-initio Simulation Package (VASP) code[38] and the Perdew-Burke-Ernzerhof (PBE)sol[39] GGA functional. Valence electrons were described by plane waves up to an energy cutoff of 400 eV and the core electrons were described within the projector augmented wave framework.[40] We used a 6×6×3 k-points grid sampling of the Brillouin zone for unit cell calculations. Final convergence criteria for the electronic wave function and geometry were 10^{-4} eV and 0.01 eV/Å, respectively. The Gaussian smearing method with a width of 0.05 eV was used to improve convergence with respect to states near the Fermi level.

3. Results and discussion

All UCNP solutions, which are highly transparent, exhibited green luminescence under IR illumination (Figure S1). Figure 1a presents the PL spectra of the Li(Gd,Y)F_4:Yb,Er UCNPs under 980 nm IR excitation (the Yb and Er concentrations were 18 and 2 mol%, respectively). The PL peaks are ascribed to the 4f-4f electronic transitions of the Er^{3+} ions via an $Yb^{3+} \rightarrow Er^{3+}$ energy transfer following the IR light absorption by the Yb^{3+} which has an absorption band at approximately 960 nm (Figure S2). The emission peaks in the green and red spectral regions result from two-photon upconversion process, as evidenced by the light power-dependent PL intensity (See Figure S3). As the Y^{3+} concentration increased to 40 mol% in the host lattice, the PL intensity increased. At higher Y^{3+} concentrations, however, the PL intensity decreased significantly. For example, 40 mol% Y^{3+}-doped $LiGdF_4$:Yb,Er ($LGY_{0.4}F$:Yb,Er) exhibited an approximately 1325 and 325-fold higher PL intensity than the 0 and 80 mol% Y^{3+}-doped $LiGdF_4$:Yb,Er UCNPs, respectively. Given the strong PL intensity ascribed to the $^4S_{3/2} \rightarrow {}^4I_{15/2}$ transition, which peaks at 550 nm, the $LGY_{0.4}F$:Yb,Er UCNPs emit a bright green light, as depicted in Figure 1b inset. Previously, Chen et al. obtained the quantum yield (QY) of $LiYF_4$:Er UCNPs by comparing with β-$NaYF_4$:Yb,Er UCNPs.[30] When the PL intensity of the $LGY_{0.4}F$:Yb,Er UCNPs was compared with that of β-$NaYF_4$:Yb,Er UCNPs, the $LGY_{0.4}F$:Yb,Er showed higher PL intensity (Figure S5). Its QY was calculated to be 0.16% by using the QY (0.1%) of β-$NaYF_4$:Yb,Er with 30 nm size.[41] Although the relative QY of the $LGY_{0.4}F$:Yb,Er UCNPs was obtained at current study, absolute QY of the $LGY_{0.4}F$:Yb,Er UCNPs will be further studied by using an integrating sphere. When we calculated intensity ratio of green to red emission ($R_{g/r}$) of the Li(Gd,Y)F_4:Yb,Er UCNPs, the $R_{g/r}$ value increased with increasing Y^{3+} concentration under the condition of 0 and 20 mol% Y^{3+} doping. In that case, particle size increased with increasing Y^{3+} concentration. On the other hand, the $R_{g/r}$ value decreased when the particle size was decreased with increasing Y^{3+} concentration (Y^{3+} concentration = 40, 60, and 80 mol%). As shown in Figure S6, $LGY_{0.4}F$:Yb,Er showed the highest $R_{g/r}$ value of 2.85. As a consequence, the $R_{g/r}$ value was dependent on the particle size and it decreased with decreasing particle size. When particle size decreases, quenching of UC luminescence induced by surface defects and ligands becomes more important and it modifies the relative population among various excited states through phonon-assisted nonradiative relaxations.[42,43] However, although edge size of the 20 mol% Y^{3+}-doped Li(Gd,Y)F_4:Yb,Er was larger than that of 60 mol% Y^{3+}-doped Li(Gd,Y)$_4$:Yb,Er, its $R_{g/r}$ value was smaller than that of the 60 mol% Y^{3+}-doped Li(Gd,Y)F_4:Yb,Er due to different crystal structure (see Figure S6). The Commission Internationale de l'Eclairage (CIE) color coordinates of the $LGY_{0.4}F$:Yb,Er UCNPs are (0.2929, 0.6917). The $LGY_{0.4}F$:Yb,Er UCNPs exhibit very high color purity of 98.9%, which is approaching that of monochromatic light due to the sharp emission peak and high green-to-red ratio in the PL intensity.

As indicated in Figure 1c, the $LGY_{0.4}F$:Yb,Er UCNPs are much larger than the other Li(Gd,Y)F_4:Yb,Er UCNPs. In addition, the X-ray diffraction (XRD) patterns presented in Figure S7 reveal the formation of an orthorhombic GdF_3 phase at doping conditions between 0 and 20 mol% Y^{3+}. The crystal structures were also verified from the UCNP lattice spacings measured via high-resolution

TEM (HR-TEM) (Figure S8). A tetragonal $LiGdF_4$ phase (the $LiYF_4$ phase for 80 mol% Y^{3+} doping) was formed at doping conditions between 40 and 80 mol% Y^{3+}. It was reported that single $LiGdF_4$ tetragonal phase is hardly synthesized and instead, GdF_3 orthorhombic phase is apt to be formed.[32] However, as the Gd^{3+} ions were replaced by Y^{3+} ions (> 20 mol%), a tetragonal phase was formed without changing the reaction temperature and/or time, which may be attributed to a decrease in the energetic barrier for the formation of a $LiGdF_4$ phase due to lanthanide doping.[33] Large size and formation of single tetragonal phase may attribute to strong UC luminescence of $LGY_{0.4}F$:Yb,Er UCNPs. It is believed that size effect is more dominant than phase effect on the luminescence, judging from similar brightness of small UCNPs corresponding to Figures 1c-i, ii, iv, and v, as shown in Figures 1 and S1b. However, further study is necessary to reveal exact origin of strong UC luminescence from $LGY_{0.4}F$:Yb,Er UCNPs. It is noted that particle size could be controlled via Ln^{3+} ion doping for the case of $LiGdF_4$ tetragonal phase, whereas it was hardly controlled for the GdF_3 orthorhombic phase. Thus, we can achieve intense UC luminescence by simply controlling the particle size when we synthesize single tetragonal $LiGdF_4$ phase. In addition, morphologies of the $Li(Gd,Y)F_4$:Yb,Er UCNPs are affected by their phases. Minute differences may be noted in the TEM images in Figure 1c. The UCNP morphologies in Figures 1c-i and 1c-ii exhibit rhombic plate-like shapes, while plate shape was not observed in Figures 1c-iii–1c-v. The particle shapes in Figures 1c-iv and 1c-v appear octahedral or truncated octahedral. This morphological difference is believed to result from their different crystal structures. The rhombic plates depicted in Figure 1c-i have edge lengths of 12.1 ± 1.0 nm and thicknesses of 4.0 ± 0.5 nm. The nanoplates are easily aligned into two-dimensional aggregates as shown in Figures 1c-i and S9 because this alignment minimizes the free energy by hydrophobic interactions of the surface ligands of the nanoplates at their largest faces.[44] As the quantity of Y^{3+} ions increased in the host lattice, the particle size decreased from 60.5 nm (edge length) for the 40 mol% Y^{3+} doping to 9.3 nm (edge length) for the 80 mol% Y^{3+} doping, which resulted in weak PL intensities for the $Li(Gd,Y)F_4$:Yb,Er. As observed in Figures 1c-iv and 1c-v, the small Li(Gd,Y)F_4:Yb,Er UCNPs appear somewhat spherical with slight faceting, while the large LGY$_{0.4}$F:Yb,Er UCNPs exhibit sharp facets.

We studied the trend in the change of the particle sizes of the Li(Gd,Y)F_4:Yb,Er UCNPs with tetragonal structure as a function of Y^{3+} concentration from 40 mol% to 80 mol%. In the high concentration regime, 60 and 80 mol% Y^{3+}, the difference in the particle size was marginally small (see Table S1 and Figure S10). However, there was significant increase in the particle size between 60 and 40 mol% Y^{3+}-doped Li(Gd,Y)F_4:Yb,Er UCNPs; the LGY$_{0.4}$F:Yb,Er UCNPs was approximately 6 times larger than the 60 mol% Y^{3+}-doped Li(Gd,Y)F_4:Yb,Er UCNPs. Previously, Wang et al. studied the size change of NaYF_4:Yb,Er UCNPs by Gd^{3+} doping by using density functional theory (DFT) calculation.[33] They found that the Gd^{3+} ions donate more electron density to adjacent F^- ions than Y^{3+} ions do leading to the increased electron polarization between cations and F^- ions. Increased electrostatic repulsive force between the electron rich F^- ions at the surface layer of NaYF_4 and F^- ions in the solution can substantially slow down the diffusion of F^- ions from solution to the nanocrystal surface. They associated this with the reduced nanocrystal size.[33] In contrast to the case of NaYF_4, the Bader charge analysis[45,46] on a unit-cell of LiYF_4, LiGdF_4, and Li(Gd$_{0.5}$,Y$_{0.5}$)F_4 (LiGdYF_4) shows that there is no significant charge redistribution upon Y^{3+} doping in bulk level as shown in Table S2. It may attribute to experimentally observed small change in size of the nanocrystals for 60 and 80 mol% Y^{3+} doping. However, in the case of similar concentrations of Y^{3+} to Gd^{3+}, upon the surface formation, some of the surface-exposed F^- ions adjacent to Y^{3+} dopants of the most stable LiGdYF_4(101) surface, which is experimentally and theoretically confirmed (see below), were less-negatively charged compared to the F^- ions in a bulk phase ($\Delta e = 0.06$). According to the discussion in Ref. 33, we postulate that these less-negatively charged F^- ions will reduce the electrostatic repulsive force upon the approach of F^- ions in solution to the LiGdYF_4(101) surface and thus can accelerate the formation of LiGdYF_4 with large size.

Previous reports indicate that LiYF_4-based nanocrystals are plate shaped.[28,32] Although a TEM image of the LGY$_{0.4}$F:Yb,Er observed along a particular crystallographic orientation (Figure 1c-iii) demonstrates a plate-like shape, the actual morphology of the $LGY_{0.4}F$:Yb,Er is octahedral as indicated in Figure 2. Figure 2a presents a TEM image of the $LGY_{0.4}F$:Yb,Er particles that were not aligned parallel to the TEM gird. No plate-shaped particles were observed in our TEM images of the $Li(Gd,Y)F_4$:Yb,Er UCNPs for 40, 60, and 80 mol% Y^{3+} doping. As demonstrated in the TEM images in Figure 2a, the central portions of the $LGY_{0.4}F$:Yb,Er UCNPs are much darker than their edges (vice versa in the HAADF STEM images, Figure S11). This severe contrast in the UCNPs indicates that the UCNPs are thicker in their centers than at the edges. The STEM and SEM studies also revealed that $LGY_{0.4}F$:Yb,Er exhibits a tetragonal bipyramidal morphology (Figures S11 and S12). The HR-TEM and HAADF HR-STEM analyses of the $LGY_{0.4}F$:Yb,Er UCTBs shown in Figure 2 proved the particles were bounded by {101} planes. The angles between two adjacent planes were measured to be 50.7 and 129.3° which are in agreement with the angles between the (101) and $(10\bar{1})$ planes of tetragonal $LiGdF_4$. The fast Fourier transform (FFT) pattern presented in the inset of Figure 2b can be indexed to be the zone axis along the [010] direction of the tetragonal $LiGdF_4$ structure. The results indicate that $LGY_{0.4}F$:Yb,Er UCTBs have a single crystalline phase with high crystallinity. To investigate the origin of the formation of tetragonal bipyramidal morphology, the surface energies of the low-index planes of $Li(Gd,Y)F_4$–(100), (101) and (111)– were calculated using density functional theory. The unit cell of $LiGdF_4$ was initially optimized and two of total for Gd^{3+} ions were substituted with Y^{3+} ions. The unit cell of $Li(Gd_{0.5},Y_{0.5})F_4$ with energetically most stable configuration of Gd^{3+} and Y^{3+} ions is presented in Figure 3a. The morphology of each plane and their surface energies are presented in Figures 3b-d and Table 1, respectively. The calculations confirm that the (101) surface is thermodynamically favored. The $LGY_{0.4}F$:Yb,Er UCTBs are faceted by eight equivalent {101} planes in a tetragonal structure, which induces a tetragonal bipyramidal morphology due to longer lattice parameter along *c*-axis. The lattice parameters, a = b = 5.177 Å and c = 10.773 Å, were calculated from the high resolution XRD pattern. All facets are atomically flat, and the two apexes along the *c*-axis are blunt (Figure S13). The tips are blunted in the cross-sectional region of approximately 20 × 20 unit cell $(uc)^2$ in the *ab* plane (Figure S13).

The Z-contrast of the atomic columns was examined in the HAADF STEM images (Figure 2e). The potential contrast variation by electron beam damage, which was observed in highly exposed areas (Figures 2c, S14, and S15), can largely be prevented by acquiring fresh STEM images. The intensity profile across XY indicates considerable variation: a higher intensity can support the existence of dopants such as Er and Yb in the Gd sites, and a lower intensity can indicate Y in Gd sites as designated by the arrows (see also Figure S14). The lanthanide elements are clearly observed in the low-pass filtered HAADF HR-STEM image (Figure 2f), and their arrangement is consistent with a projection of $LiGdF_4$ unit cell in the [010] direction. The $LiGdF_4$ has a scheelite structure ($I4_1/a$, Z = 4), and the Li^+ and Gd^{3+} ions are four-fold and eight-fold coordinated by the F^- ions, respectively (Figure 2d).[47,48] It should be noted that the Li and F atoms are not visible in the HAADF STEM image in Figure 2f because they are very light in comparison with the Y^{3+} and Ln^{3+} ions.

The elemental distribution within a nanoparticle was examined using an EELS-based EFTEM technique. For the materials containing Li, such as our $LGY_{0.4}F$:Yb,Er UCTBs, EELS analysis is a powerful tool because, unlike EDS, it can detect light elements such as Li. Additionally, EFTEM provides rapid elemental mapping for electron-beam-sensitive materials. Figure 4 presents an elastic TEM image and thickness map of the $LGY_{0.4}F$:Yb,Er UCTBs and the corresponding elemental maps. The core-loss EELS spectra of the Li-K, Gd-$M_{4,5}$, Y-$L_{2,3}$, F-K, Yb-$M_{4,5}$, and Er-$M_{4,5}$ maps obtained from the $LGY_{0.4}F$:Yb,Er UCTBs are presented in Figure S16. Acquiring the high energy-loss spectra in TEM (above approximately 1500 eV) is challenging due to the small signal-to-noise ratio. Surprisingly, however, the core-loss edges such as the Gd-$M_{4,5}$ (1185 eV), Er-$M_{4,5}$ (1409 eV), Yb-$M_{4,5}$ (1528 eV) and even the Y-$L_{2,3}$ (2080 eV) edges were successfully acquired with the enhanced signal-to-noise ratio and collection efficiency of the GIF Quantum®ERS (Gatan, Inc., Pleasanton, CA, USA). As a result, EFTEM maps from all elements including lanthanide elements could be successfully obtained as shown in Figure 4. One thing to note is that the sharp features observed in the image of Figure 4a are not observed in the Gd, Y, and Yb EFTEM images of Figure 4c which appear more rounded due to low signal intensity at thin regions such as the apex and the edge of this bipyramidal nanocrystal (see thickness map of Figure 4b), particularly for high energy-loss peaks (above 1000 eV). Excepting this smoothing effect, however, one can notice that all elements are uniformly distributed over a single UCTB. Even the quantity of the activator Er^{3+} ion is very small, existence of Er^{3+} ions over a particle is clearly seen.

The as-synthesized $LGY_{0.4}F$:Yb,Er UCTBs were highly uniform in size and shape (60.5 ± 1.6 nm × 55.3 ± 1.4 nm), which allows for two-dimensional (2D) ordered arrangement of $LGY_{0.4}F$:Yb,Er UCTBs (Figures 5a and S11b). When the size of the UCTBs decreased due to slight increase of Y^{3+} concentration in the host lattice, an even higher ordered 2D superlattice could be obtained (Figures 5b-d). The $Li(Gd_{0.35}Y_{0.45})F_4$:Yb,Er ($LGY_{0.45}F$:Yb,Er) also exhibits a single tetragonal phase with high crystallinity (Figure S17). The slow evaporation of the solvent allows the $LGY_{0.45}F$:Yb,Er UCTBs to assemble into 2D monolayers in which the {101} planes of the UCTBs are parallel to the TEM grid. The spotty selected area electron diffraction (SAED) pattern supports a highly ordered UCTB assembly. The HAADF STEM image of Figure 5d confirms that the smaller $LGY_{0.45}F$:Yb,Er constituting the 2D superlattice also has a bipyramidal shape. The bright contrast at the apexes results from the overlap of apexes of adjacent particles.

The feasibility of applying $LGY_{0.4}F$:Yb,Er UCTBs to transparent volumetric three-dimensional (3D) displays was investigated by incorporating UCTBs into a polydimethylsiloxane (PDMS) polymer. Although these UCTBs have an anisotropic morphology and are larger than the previously reported NPs that were successfully incorporated into a PDMS polymer,[33] they were well-dispersed in the PDMS polymer, which allowed for the fabrication of highly transparent UCTB-PDMS composites (Figure 6). The transmittance of the UCTB-PDMS composites was found to exceed 90% in the visible spectral region (Figure 6a). As indicated in photographs of the $LGY_{0.4}F$:Yb,Er UCTB-PDMS bar and disk in Figure 6c, the luminescence is homogenous, bright green and sufficiently intense to render characters on the background paper legible. The high transparency and brightness of the UCTB-PDMS composites can be attributed to the strong UC luminescence from the $LGY_{0.4}F$:Yb,Er UCTBs which allows small quantities of the UCTBs to mix with PDMS. These results also indicate that the UCTBs have the potential for applications in volumetric 3D displays.[1,33]

4. Conclusions

In summary, we demonstrated a pathway for achieving highly bright $LiGdF_4$:Yb,Er UCNPs via Y^{3+} doping. We found that Y^{3+} doping initiated the formation of a tetragonal phase and affected the particle size. Single tetragonal-phase $Li(Gd,Y)F_4$:Yb,Er UCNPs with Y^{3+} concentrations similar to the Gd^{3+} concentration exhibited intense UC green luminescence and tetragonal bipyramid morphologies. Additionally, sub-10 nm ultrasmall UCTBs could be obtained via Y^{3+} doping. Uniform distribution of all constituent elements of $LGY_{0.4}F$:Yb,Er UCTBs was directly seen via EFTEM mapping. These $LGY_{0.4}F$:Yb,Er UCTBs were also successfully incorporated into and uniformly distributed throughout PDMS polymer composites. The strong UC luminescence of the $LGY_{0.4}F$:Yb,Er allowed the fabrication of highly transparent and bright green-emitting PDMS composites. These $Li(Gd,Y)F_4$:Yb,Er materials are potentially applicable in the highly desired transparent volumetric 3D displays.

Acknowledgements

This work was supported in part by the Dream project (2V03410) funded by the Korea Institute of Science and Technology (KIST), the MRSEC Program of the National Science Foundation (NSF) under Award Number DMR-0819885, and the U.S. Department of Energy, Office of Basic Energy Sciences, under Contract DE-AC02-98CH10886 (H.Y.K.), and parts of this work were carried out in the Characterization Facility, University of Minnesota, which receives partial support from NSF through the MRSEC program. We thank Seo Kyoung Ryu and Min Kyoung Cho for her technical help for EFTEM analysis (2V02951).

References

1 H. Na, K. Woo, K. Lim and H. S. Jang, *Nanoscale*, 2013, **5**, 4242.

2 Z. Li and Y. Zhang, *Angew. Chem. Int. Ed.*, 2006, **45**, 7732.

3 F. Zhang, Y. Wan, T. Yu, F. Zhang, Y. Shi, S. Xie, Y. Li, L. Xu, B. Tu and D. Zhao, *Angew. Chem. Int. Ed.*, 2007, **46**, 7976.

4 H. S. Jang, H. Yang, S. W. Kim, J. Y. Han, S.-G. Lee and D. Y. Jeon, *Adv. Mater.*, 2008, **20**, 2696.

5 C. Feldmann, T. Justel, C. R. Ronda and D. U. Wiechert, *J. Lumin.*, 2001, **92**, 245.

6 H. S. Jang, H. Y. Kim, Y.-S. Kim, H. M. Lee and D. Y. Jeon, *Opt. Express*, 2012, **20**, 2761.

7 S. Y. Kim, K. Woo, K. Lim, K. Lee and H. S. Jang, *Nanoscale*, 2013, **5**, 9255.

8 H. S. Jang, K. Woo and K. Lim, *Opt. Express*, 2012, **20**, 17107.

9 P. Li, Q. Peng and Y. D. Li, *Adv. Mater.*, 2009, **21**, 1945.

10 Y. Liu, D. Tu, H. Zhu, R. Li, W. Luo and X. Chen, *Adv. Mater.*, 2010, **22**, 3266.

11 Y. Liu, K. Ai, J. Liu, Q. Yuan, Y. He and L. Lu, *Angew. Chem. Int. Ed.*, 2012, **51**, 1437.

12 Y. Liu, D. Wang, J. Shi, Q. Peng and Y. Li, *Angew. Chem. Int. Ed.*, 2013, **52**, 4366.

13 R. Kumar, M. Nyk, T. Y. Ohulchanskyy, C. A. Flask and P. N. Prasad, *Adv. Funct. Mater.*, 2009, **19**, 853.

14 S. Wu, G. Han, D. J. Milliron, S. Aloni, V. Altoe, D. V. Talapin, B. E. Cohen and P. J. Schuck, *Proc. Natl. Acad. Sci. U. S. A.*, 2009, **106**, 10917.

15 M. Haase, S. Heer, K. Kömpe and H. U. Güdel, *Adv. Mater.*, 2004, **16**, 2102.

16 N. J. J. Johnson, W. Oakden, G. J. Stanisz, R. S. Prosser and F. C. J. M. van Veggel, *Chem. Mater.*, 2011, **23**, 3714.

17 Q. Liu, Y. Sun, T. Yang, W. Feng, C. Li and F. Li, *J. Am. Chem. Soc.*, 2011, **133**, 17122.

18 F. Wang, J. Wang, J. Xu, X. Xue, H. Chen and X. Liu, *Spectr. Lett.*, 2010, **43**, 400.

19 E. van der Kolk, P. Dorenbos, K. Kramer, D. Biner and H. U. Gudel, *Phys. Rev. B*, 2008, **77**, 125110.

20 G. Chen, J. Shen, T. Y. Ohulchanskyy, N. J. Patel, A. Kutikov, Z. Li, J. Song, R. K. Pandey, H. Agren, P. N. Prasad and G. Han, *ACS Nano*, 2012, **6**, 8280.

21 H.-X. Mai, Y.-W. Zhang, R. Si, Z.-G. Yan, L.-D. Sun, L.-P. You and C.-H. Yan, *J. Am. Chem. Soc.*, 2006, **128**, 6426.

22 L. W. Yang, Y. Li, Y. C. Li, J. J. Li, J. H. Hao, J. X. Zhong and P. K. Chu, *J. Mater. Chem.*, 2012, **22**, 2254.

23 Q. Cheng, J. Sui and W. Cai, *Nanoscale*, 2012, **4**, 779.

24 G. Chen, T. Y. Ohulchanskyy, W. C. Law, H. Agren and P. N. Prasad, *Nanoscale*, 2011, **3**, 2003.

25 R. Naccache, F. Vetrone, V. Mahalingam, L. A. Cuccia and J. A. Capobianco, *Chem. Mater.*, 2009, **21**, 717.

26 K. W. Krämer, D. Biner, G. Frei, H. U. Güdel, M. P. Hehlen and S. R. Lüthi, *Chem. Mater.*, 2004, **16**, 1244.

27 R. T. Wegh, H. Donker, K. D. Oskam and A. Meijerink, *Science*, 1999, **283**, 663.

28 V. Mahalingam, F. Vetrone, R. Naccache, A. Speghini and J. A. Capobianco, *Adv. Mater.*, 2009, **21**, 4025.

29 J. Wang, F. Wang, J. Xu, Y. Wang, Y. Liu, X. Chen, H. Chen and X. Liu, *C. R. Chim.*, 2010, **13**, 731.

30 G. Chen, T. Y. Ohulchanskyy, A. Kachynski, H. Agren and P. N. Prasad, *ACS Nano*, 2011, **5**, 4981.

31 V. Mahalingam, R. Naccache, F. Vetrone and J. A. Capobianco, *Chem.-Eur. J.*, 2009, **15**, 9660.

32 Y.-P. Du, Y.-W. Zhang, L.-D. Sun and C.-H. Yan, *Dalton Trans.*, 2009, 8574.

33 F. Wang, Y. Han, C. S. Lim, Y. Lu, J. Wang, J. Xu, H. Chen, C. Zhang, M. Hong and X. Liu, *Nature*, 2010, **463**, 1061.

34 F. Wang, J. Wang and X. Liu, *Angew. Chem. Int. Ed.*, 2010, **49**, 7456.

35 Q. Su, S. Han, X. Xie, H. Zhu, H. Chen, C.-K. Chen, R.-S. Liu, X. Chen, F. Wang and X. Liu, *J. Am. Chem. Soc.*, 2012, **134**, 20849.

36 C. Dong, J. Pichaandi, T. Regier and F. C. J. M. van Veggel, *J. Phys. Chem. C*, 2011, **115**, 15950.

37 J. Park, K. J. An, Y. Hwang, J.-G. Park, H.-J. Noh, J.-Y. Kim, J.-H. Park, N.-M. Hwang and T. Hyeon, *Nat. Mater.*, 2004, **3**, 891.

38 G. Kresse and J. Furthmüller, *Phys. Rev. B*, 1996, **54**, 11169.

39 J. P. Perdew, A. Ruzsinszky, G. I. Csonka, O. A. Vydrov, G. E. Scuseria, L. A. Constantin, X. Zhou and K. Burke, *Phys. Rev. Lett.*, 2008, **100**, 136406.

40 P. E. Blöchl, *Phys. Rev. B*, 1994, **50**, 17953.

41 J.-C. Boyer and F. C. J. M. van Veggel, *Nanoscale*, 2010, **2**, 1417.

42 H. X. Mai, Y. W. Zhang, L. D. Sun and C. H. Yan, *J. Phys. Chem. C*, 2007, **111**, 13721.

43 X. Ye, J. E. Collins, Y. Kang, J. Chen, D. T. N. Chen, A. G. Yodh and C. B. Murray, *Prod. Natl. Acad. Sci. U. S. A.*, 2010, **107**, 22430.

44 H. Wang and T. Nann, *Nanoscale Res. Lett.*, 2011, **6**, 267.

45 G. Henkelman, A. Arnaldsson and H. Jónsson, *Comput. Mater. Sci.*, 2006, **36**, 354.

46 W. Tang, E. Sanville and G. Henkelman, *J. Phys.-Condes. Matter*, 2009, **21**, 084204.

47 R. E. Thoma, G. D. Brunton, R. A. Penneman and T. K. Keenan, *Inorg. Chem.*, 1970, **9**, 1096.

48 A. V. Goryunov, A. I. Popov, N. M. Khajdukov and P. P. Fedorov, *Mater. Res. Bull.*, 1992, **27**, 213.

Figure Captions

Fig. 1 (a) PL spectra, (b) CIE color coordinates, and (c) TEM images of Li(Gd,Y)F_4:Yb,Er UCNPs. [i: Y = 0 mol%, ii: Y = 20 mol%, iii: Y = 40 mol%, iv: Y = 60 mol%, v: Y = 80 mol%] Inset in (a) shows magnified PL spectra of low PL intensity region. Inset in (b) shows luminescent LG$Y_{0.4}$F:Yb,Er UCNP solutions (~ 1 wt%) under the irradiation of 980 nm IR diode laser. [I: $^4G_{11/2}\rightarrow{}^4I_{15/2}$, II: $^2H_{9/2}\rightarrow{}^5I_{15/2}$, III: $^4F_{7/2}\rightarrow{}^4I_{15/2}$, IV: $^2H_{11/2}\rightarrow{}^4I_{15/2}$, V: $^4S_{3/2}\rightarrow{}^4I_{15/2}$, VI: $^4F_{9/2}\rightarrow{}^4I_{15/2}$, VII: $^4I_{9/2}\rightarrow{}^4I_{15/2}$, VIII: $^4S_{3/2}\rightarrow{}^4I_{9/2}$]

Fig. 2 (a) Bright-field TEM, (b) HR-TEM, and (c) HAADF STEM images, (d) perspective view of LG$Y_{0.4}$F:Yb,Er unit cell structure, (e) HAADF HR-STEM and (f) filtered HAADF HR-STEM images of LG$Y_{0.4}$F:Yb,Er UCTBs. Inset in (a) shows a schematic diagram of the crystal morphology and inset of (b) indicates FFT diffractogram for the HR-TEM image. Inset in (e) indicates Z-contrast intensity profile across line XY. [010]-projection of the unit cell was superimposed in (f) filtered HAADF HR-STEM image of LG$Y_{0.4}$F:Yb,Er UCTBs.

Fig. 3 Morphology of Li($Gd_{0.5}Y_{0.5}$)F_4 host crystal: (a) a single unit cell, (b) a 3×2×1 supercell of the (100) plane, (c) a 2×3×1 supercell of the (101) plane, and (d) a 3×2×1 supercell of the (111) plane.

Fig. 4 (a) Elastic TEM image and (b) thickness map of LG$Y_{0.4}$F:Yb,Er UCTBs. (c) EFTEM elemental maps for (i) Li, (ii) Gd, (iii) Y, (iv) F, (v) Yb, and (vi) Er are shown.

Fig. 5 (a) TEM image of LG$Y_{0.4}$F:Yb,Er, (b, c) TEM and (d) STEM images of LG$Y_{0.45}$F:Yb,Er UCTBs. Inset in (c) shows a corresponding SAED pattern showing diffraction spots resulting from superlattice of the LG$Y_{0.45}$F:Yb,Er UCTBs.

Fig. 6 (a) Transmittance spectrum of LG$Y_{0.4}$F:Yb,Er UCTB-PDMS bar and digital camera images of LG$Y_{0.4}$F:Yb,Er UCTB-PDMS bar (left) and disk (right) under (b) ambient conditions and (c) IR light irradiation.

Table list

Table 1. DFT calculated surface energies of (100), (101), and (111) planes of Li($Gd_{0.5}Y_{0.5}$)F_4 host crystal.

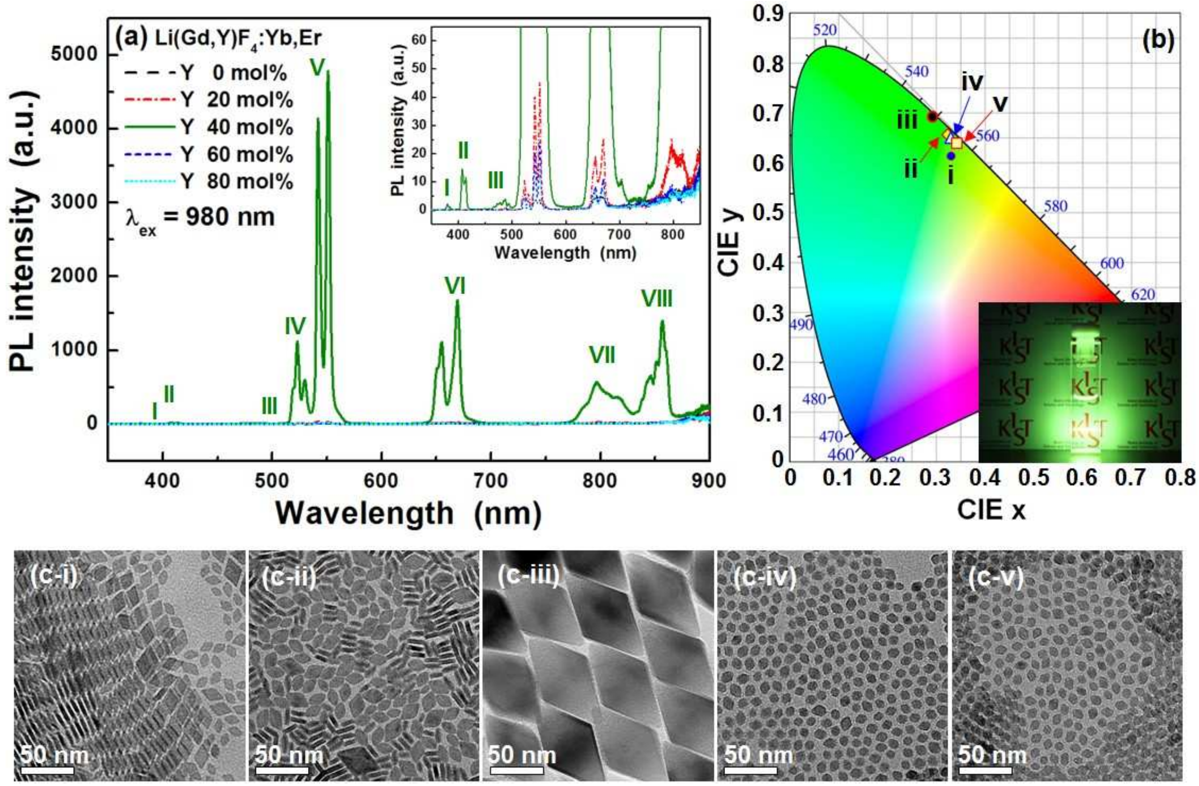

Fig. 1 (a) PL spectra, (b) CIE color coordinates, and (c) TEM images of Li(Gd,Y)F_4:Yb,Er UCNPs. [i: Y = 0 mol%, ii: Y = 20 mol%, iii: Y = 40 mol%, iv: Y = 60 mol%, v: Y = 80 mol%] Inset in (a) shows magnified PL spectra of low PL intensity region. Inset in (b) shows luminescent LG$Y_{0.4}$F:Yb,Er UCNP solutions (~ 1 wt%) under the irradiation of 980 nm IR diode laser. [I: $^4G_{11/2}\rightarrow{}^4I_{15/2}$, II: $^2H_{9/2}\rightarrow{}^5I_{15/2}$, III: $^4F_{7/2}\rightarrow{}^4I_{15/2}$, IV: $^2H_{11/2}\rightarrow{}^4I_{15/2}$, V: $^4S_{3/2}\rightarrow{}^4I_{15/2}$, VI: $^4F_{9/2}\rightarrow{}^4I_{15/2}$, VII: $^4I_{9/2}\rightarrow{}^4I_{15/2}$, VIII: $^4S_{3/2}\rightarrow{}^4I_{9/2}$]

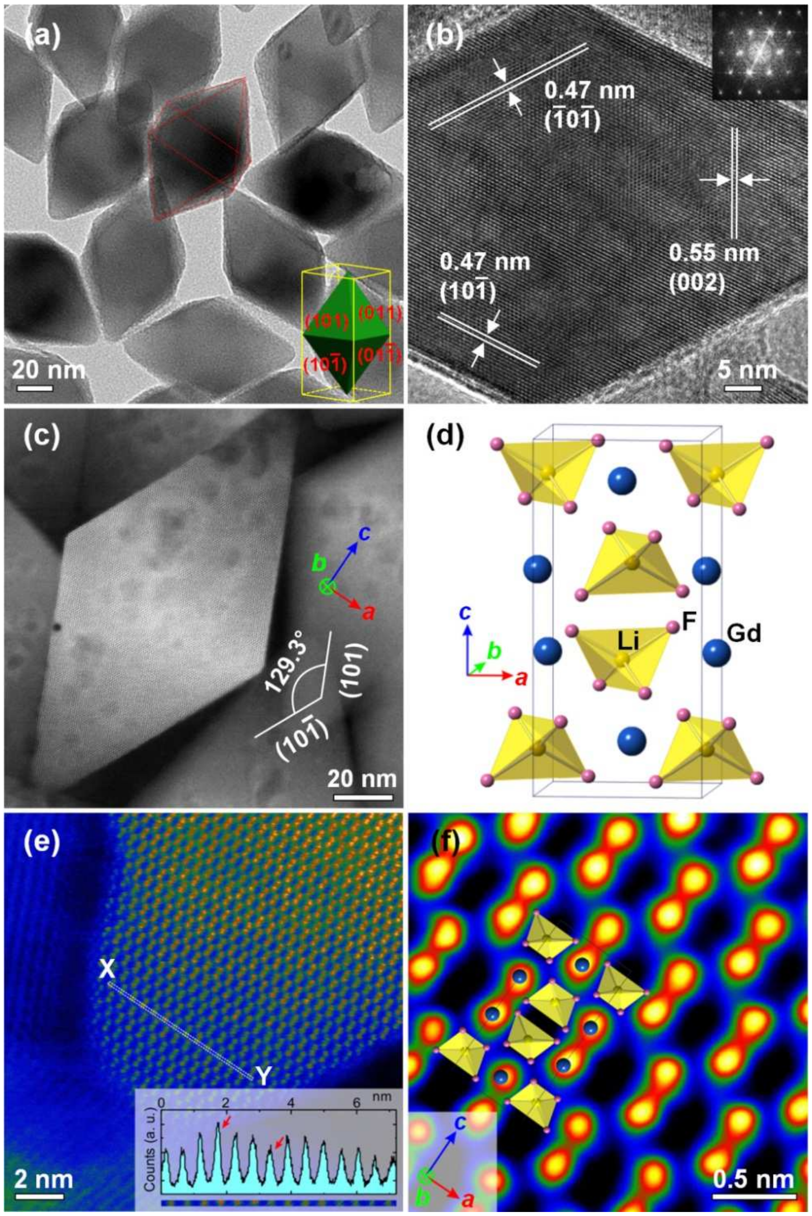

Fig. 2 (a) Bright-field TEM, (b) HR-TEM, and (c) HAADF STEM images, (d) perspective view of LGY$_{0.4}$F:Yb,Er unit cell structure, (e) HAADF HR-STEM and (f) filtered HAADF HR-STEM images of LGY$_{0.4}$F:Yb,Er UCTBs. Inset in (a) shows a schematic diagram of the crystal morphology and inset of (b) indicates FFT diffractogram for the HR-TEM image. Inset in (e) indicates Z-contrast intensity profile across line XY. [010]-projection of the unit cell was superimposed in (f) filtered HAADF HR-STEM image of LGY$_{0.4}$F:Yb,Er UCTBs.

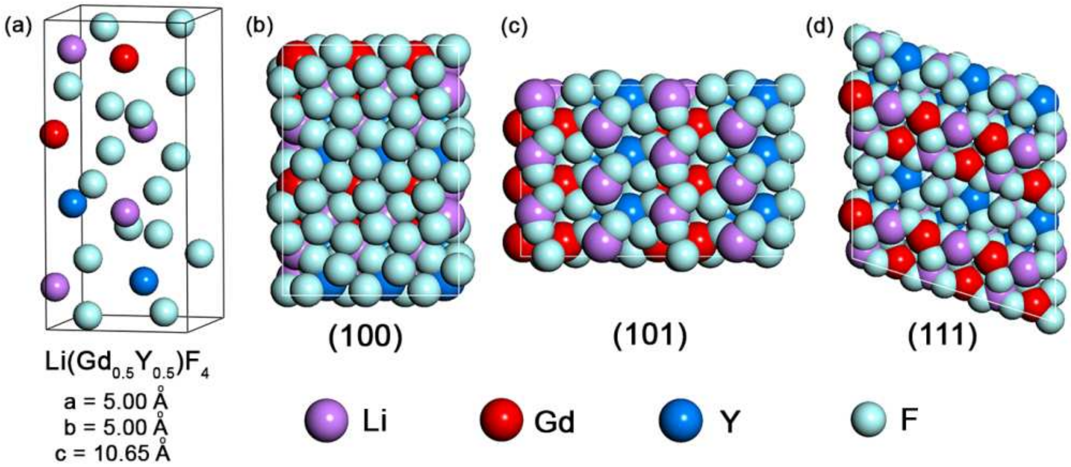

Fig. 3 Morphology of Li($Gd_{0.5}Y_{0.5}$)F_4 host crystal: (a) a single unit cell, (b) a 3×2×1 supercell of the (100) plane, (c) a 2×3×1 supercell of the (101) plane, and (d) a 3×2×1 supercell of the (111) plane.

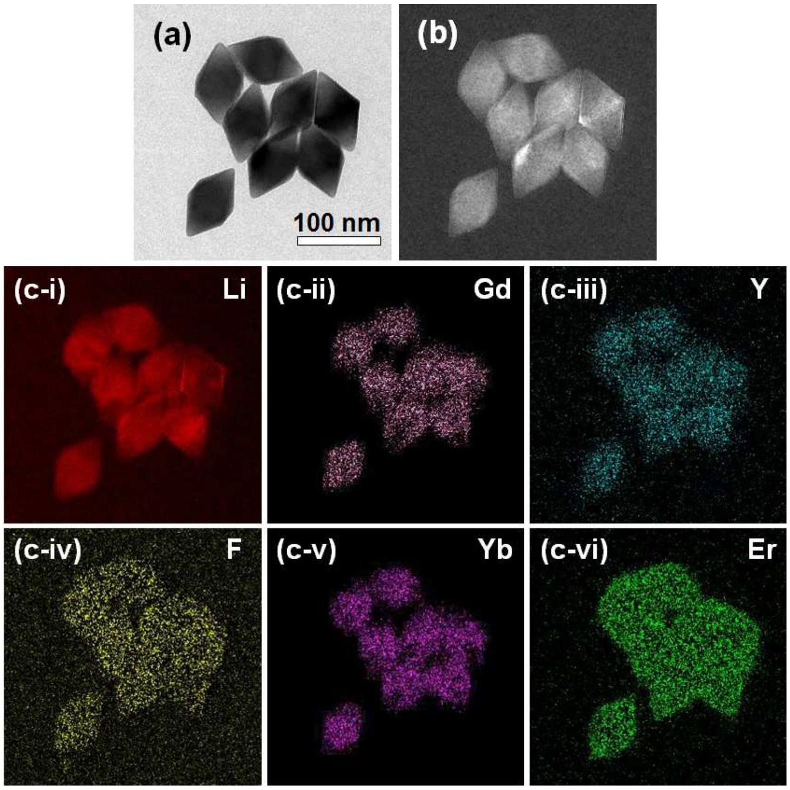

Fig. 4 (a) Elastic TEM image and (b) thickness map of LGY$_{0.4}$F:Yb,Er UCTBs. (c) EFTEM elemental maps for (i) Li, (ii) Gd, (iii) Y, (iv) F, (v) Yb, and (vi) Er are shown.

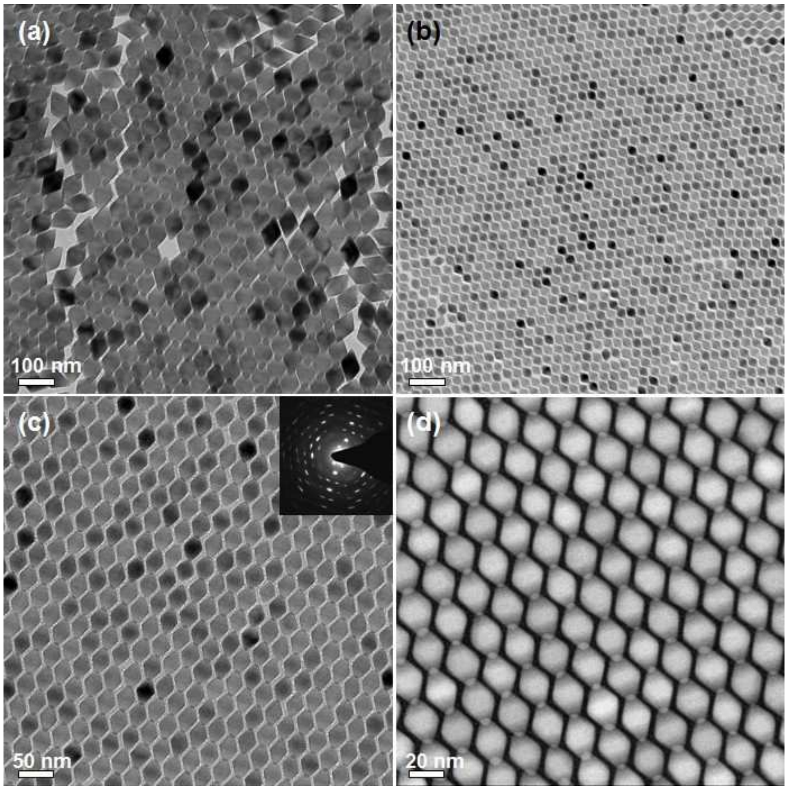

Fig. 5 (a) TEM image of $LGY_{0.4}F$:Yb,Er, (b, c) TEM and (d) STEM images of $LGY_{0.45}F$:Yb,Er UCTBs. Inset in (c) shows a corresponding SAED pattern showing diffraction spots resulting from superlattice of the $LGY_{0.45}F$:Yb,Er UCTBs.

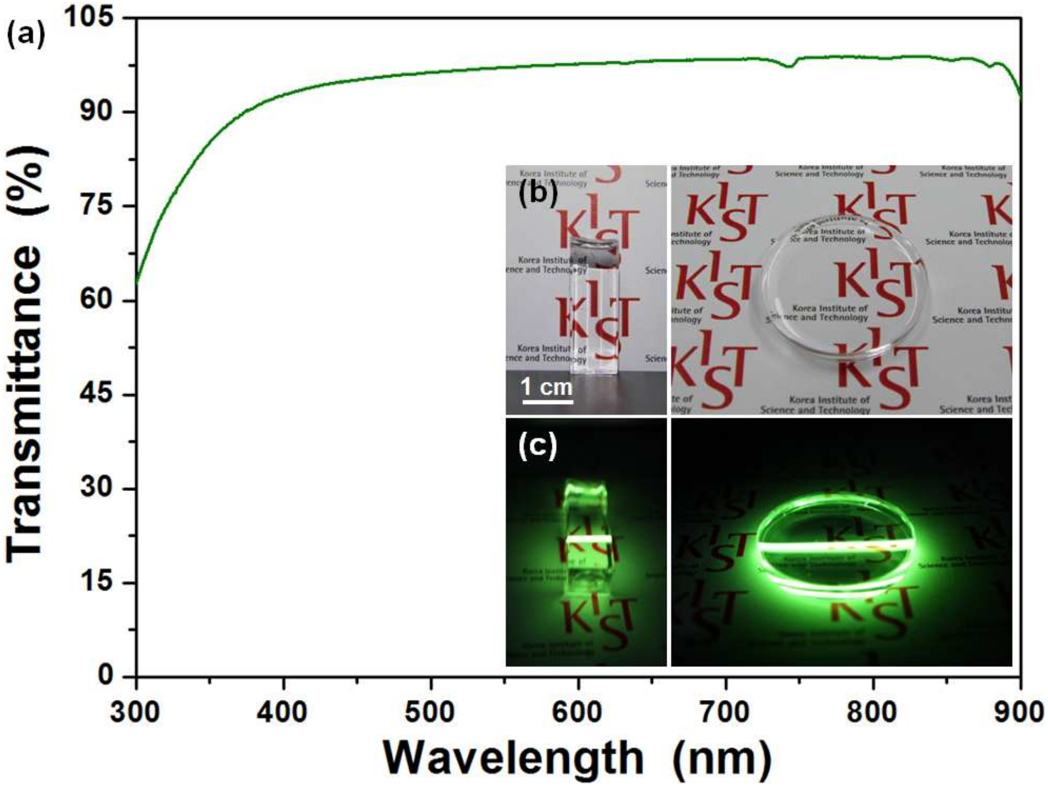

Fig. 6 (a) Transmittance spectrum of $LGY_{0.4}F$:Yb,Er UCTB-PDMS bar and digital camera images of $LGY_{0.4}F$:Yb,Er UCTB-PDMS bar (left) and disk (right) under (b) ambient conditions and (c) IR light irradiation.

Table 1. DFT calculated surface energies of (100), (101), and (111) planes of $Li(Gd_{0.5}Y_{0.5})F_4$ host crystal.

Surface index	(100)	(101)	(111)
Surface energy (eV/Å^2)	0.418	0.051	0.098
Surface energy (J/m^2)	6.67	0.82	1.57

TOC

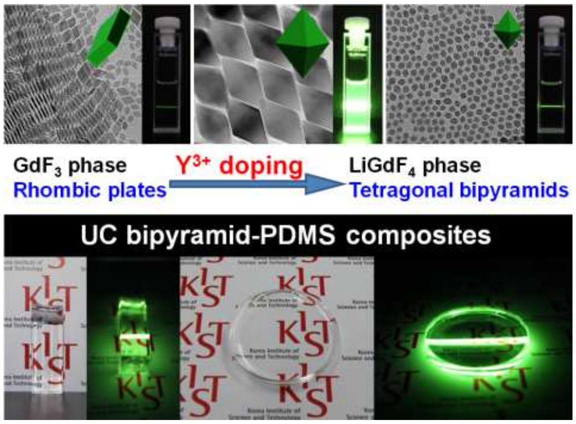

Intense upconversion green-emitting LiGdF$_4$:Yb,Er-based tetragonal bipyramidal nanophosphors are synthesized via Y^{3+} doping. Crystal phase and particle size of LiGdF$_4$:Yb,Er are simultaneously controlled via Y^{3+} doping. The highly transparent Li(Gd,Y)F$_4$:Yb,Er upconversion bipyramid-polydimethlysiloxane composites are prepared and they emit bright green light under infrared irradiation.